Journal of the Chinese Chemical Society

RESEARCH ARTICLE

A Flexible Indolocarbazole Ligand Platform for Tunable Multinuclear Metal Complexes

Cristina Decavoli[1] | Jana Jelušić[1] | Sebastian M. Krajewski[2] | Victor S. Batista[1] | Gary W. Brudvig[1]

[1]Department of Chemistry and Energy Sciences Institute, Yale University, New Haven, Connecticut, USA | [2]Department of Chemistry and Chemical and Biophysical Instrumentation Center, Yale University, New Haven, Connecticut, USA

Correspondence: Gary W. Brudvig (gary.brudvig@yale.edu)

Received: 23 February 2026 | **Revised:** 29 March 2026 | **Accepted:** 1 April 2026

Keywords: copper | dinuclear | iridium | rotational freedom | solar fuels | tetranuclear

ABSTRACT

We introduce a flexible indolocarbazole-based ligand platform for constructing multinuclear metal complexes with tunable metal–metal separations and donor strength. The platform is functionalized with two 2-(2′-pyridyl)-2-propanoate units. This architecture provides rotational freedom that enables access to multiple coordination geometries, while deprotonation modulates ligand donor power. Coordination to iridium affords a tetracarbonyl diiridium complex with an Ir···Ir distance of 4.6 Å; computational studies indicate that μ-oxo incorporation could contract this separation to values relevant for high-valent iridium water oxidation catalysts. In contrast, copper coordination yields a tetranuclear solid-state assembly that dissociates into dinuclear units in solution and features a well-defined molecular pocket with Cu–Cu separations reminiscent of methanotrophic enzyme active sites. Although steric and oxidative limitations currently restrict catalytic activity, the ligand framework's ability to enforce specific metal–metal distances and encapsulate small molecules highlights its promise as a modular platform for multinuclear catalysis and gas-binding applications.

1 | Introduction

The ligand 2-(2′-pyridyl)-2-propanoate, pyalk, has proved highly effective in oxidation catalysis [1, 2]. Its alkoxide functionality facilitates proton-coupled electron transfer (PCET), while strong σ- and π-donor properties stabilize unusually high-valent metal oxidation states. The pyridine unit, featuring a dimethyl-protected benzylic position, provides robust metal binding and resistance to ligand degradation under oxidative catalytic conditions. Pyalk also exhibits broad solubility in both aqueous and nonaqueous media and generates an anisotropic ligand field that enhances the geometry-dependent redox behavior.

Our group has extensively investigated pyalk-supported oxidation catalysts across a range of metal centers (Mn, Cu, Ni, and Ir), consistently observing effective oxidation activity [3–8]. Among these systems, Ir and Cu complexes display particularly strong performance in water oxidation. Ir-pyalk complexes give rise to the so-called “Blue Solution”: a homogeneous deep purple-blue solution (λ_{max} ~ 610 nm) containing molecular iridium dimers that catalyze water oxidation efficiently under acidic conditions [9, 10]. Formation of the Blue Solution requires bidentate ligand coordination, while monodentate binding favors the formation of iridium oxide nanoparticles under oxidative activation. The Blue Solution comprises a mixture of regio- and structural isomers with varying catalytic activities. Combined experimental and computational studies have proposed the active species to be a μ-oxo bridged Ir(IV) dimer with an Ir···Ir separation of approximately 3.5 Å, each metal center coordinated by a single pyalk ligand; however, no crystal structure of an active isomer has yet been obtained [11, 12]. Current efforts are, therefore, focused on minimizing isomer formation to increase the population of a single active species amenable to crystallization.

Copper pyalk complexes offer a complementary and earth-abundant alternative, with superior water oxidation activity at

https://doi.org/10.1002/jccs.70197

pH > 10.5 when compared to Ir complexes, with an overpotential of only 550 mV and a turnover frequency of $0.7\,s^{-1}$ [5]. These catalysts retained robust stability with ~80% activity after 12 h of continuous electrolysis, achieving more than 30 catalytic turnovers. Mechanistic studies combining experiment and computation established a mononuclear catalytic pathway involving ligand rearrangement to generate a substrate-binding site [13]. A dinuclear mechanism was excluded based on the linear dependence of peak catalytic current on catalyst concentration in cyclic voltammetry, consistent with the short-lived oxyl radical intermediates favoring mononuclear reactivity. Nevertheless, the potential role of cooperative effects between proximal catalyst molecules remains an open question.

To suppress isomer formation in the Blue Solution and to probe possible cooperative dinuclear reactivity in Cu-pyalk systems, we designed a rigid, oxidation-resistant organic scaffold capable of maintaining two metal centers at a target separation of ~3.5 Å, thereby promoting μ-oxo bridge formation upon oxidation. This scaffold consists of a planar indolocarbazole framework bearing pyalk-functionalized nitrogen atoms (Figure 1). Rotation about the C_{py}-N_{ic} bond (py = pyalk, ic = indolocarbazole) allows each pyalk unit to independently coordinate a metal center while modulating the metal–metal distance.

Here, we report the synthesis and characterization of this dimeric ligand and its complexes with Ir and Cu. For Ir, the tetracarbonyl precatalyst was structurally characterized, with its crystal structure revealing an Ir···Ir distance of 4.6 Å; computational analysis indicates sufficient flexibility to accommodate μ-oxo formation at 3.5 Å, consistent with the proposed active Blue Solution isomer. In contrast, Cu coordination yields a tetranuclear cluster in the solid state, in which two orthogonal ligand scaffolds bind four Cu centers, with pyalk hydroxyl groups bridging pairs of Cu ions at ~3.0 Å. This assembly creates an internal cavity with Cu···Cu separations of 5.3–5.7 Å, suggesting potential applications in catalysis or gas absorption; solution studies reveal dissociation into dinuclear species, eliminating the cavity and rendering the Cu centers within each ligand effectively independent.

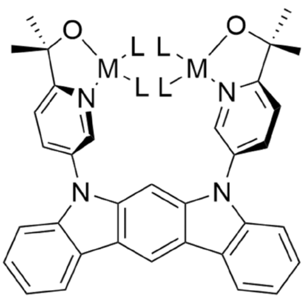

FIGURE 1 | Molecular structure of the investigated molecules, where M = Ir, Cu and L = CO, AcO⁻.

2 | Results and Discussion

2.1 | Molecular Design and Synthesis

The indolocarbazole scaffold exhibits a carbazole N...carbazole N distance of approximately 5 Å and provides a convenient platform for symmetrical functionalization at both nitrogen atoms [14, 15]. The incorporation of two pyalk substituents, which possess rotational freedom around the C_{py}-N_{ic} bond, enables the ligand to adopt fewer conformational geometries than in the untethered case. The rotational flexibility results in pyridine N...pyridine N distances ranging from 4.2 to 6.85 Å, accommodating metal centers with varying coordination requirements. The conformational freedom of the pyalk units also permits stabilization of structures in which the metal centers are positioned on opposite faces of the indolocarbazole plane. Importantly, the dihedral angle between the pyalk moieties and the indolocarbazole core effectively inhibits charge transfer through the scaffold, thereby minimizing electronic coupling between the spatially separated metal centers.

The **ICDPyalk** ligand was synthesized through a two-step synthesis (Figure 2). First, the microwave-assisted copper-catalyzed *pseudo*-Ullmann coupling of 5,7-dihydroindolo[2,3-b]carbazole with 1-(5-bromopyridin-2-yl)ethanone inserted the pyridinyl pendants on the indolocarbazole scaffold [16]. Subsequent treatment with Grignard reagent in tetrahydrofuran for 2 h introduced the alcohol functionalities, yielding a pale yellowish solid. The product was purified by column chromatography followed by recrystallization from EtOAc:hexanes (2:1) to afford the **ICDPyalk** ligand (**2**).

For iridium complexation, **ICDPyalk** (**2**) was dissolved in dichloromethane with freshly purified $[Ir(cod)(OMe)]_2$ (cod = 1,5-cyclooctadiene) and stirred for 1 h (Figure 3). Bubbling CO through the solution for 15 min generated the tetracarbonyl precatalyst **[Ir$_2$(ICDPyalk)(CO)$_4$]** (**3**) as a brown

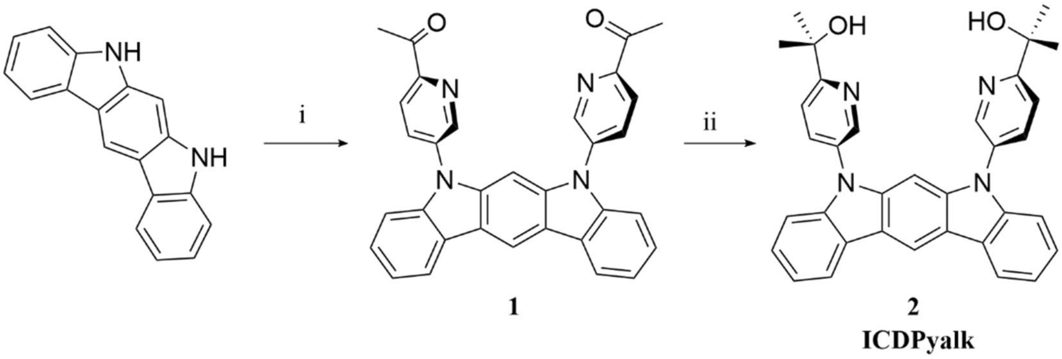

FIGURE 2 | Synthetic pathway for **2**. (i) 1-(5-Bromopyridin-2-yl)ethenone, copper iodide, cesium carbonate, *N*,*N*-dimethylformamide, microwave, 200°C, 60 min, 200 W. (ii) methylmagnesiumbromide, THF, 30°C, 2 h.

solid. Layering of *n*-octane onto a dichloromethane solution of **3** at −20°C under nitrogen atmosphere for 1 day gave delicate pale-yellow crystals. The precatalyst exhibits bench stability for several days but is best stored in the freezer. For copper complexation, **ICDPyalk** was treated with $Cu(OAc)_2•4H_2O$ in a $CHCl_3$/MeOH/MeCN solvent mixture (Figure 3). After stirring overnight at room temperature and removing the solvents, the resulting bluish-green solid was redissolved in $CHCl_3$ and filtered with a 0.2 µm PTFE (polytetrafluoroethylene) membrane filter to remove insoluble material. Crystallization via vapor diffusion of pentane at −20°C over 1 week yielded blue crystals corresponding to the tetranuclear copper complex **$[Cu_4(ICDPyalk)_2(OAc)_4]$** formed by two subunits of **$[Cu_2(ICDPyalk)(OAc)_2(L)_2]$** (**4**), where L represents a neutral ligand, such as water or methanol, necessary to achieve the square-planar geometry typical of Cu(II) complexes.

2.2 | X-Ray Diffraction Characterization

The crystals obtained with complexes **3** and **4** have been analyzed with X-ray diffraction (XRD). For complex **3**, the XRD data show two distorted square-planar iridium centers coordinated with the pyalk ligands and two carbonyls (Figure 4). The molecules are packed via π-stacking of the three central rings of the indolocarbazole scaffold and a weak hydrogen bonding of the methyl groups with the basic pyalk oxygen atoms (3.7 Å). The packing of the indolocarbazole scaffolds is not exactly parallel and the distances between two different molecules range from 3.3 to 4.3 Å. These findings are reflected in the physical properties of the crystals, which exhibited thermal instability at room temperature and demonstrated mechanical fragility, readily fracturing into smaller fragments. Interestingly, in each molecule, the two iridium centers face each other with only 4.36 Å distance, a value close to the target distance for Blue Solution species [11]. The crystal structure of complex **4** reveals four copper centers with distinct coordination geometries: three adopt distorted square pyramidal configurations with apical water ligands at 2.4 Å, while the fourth exhibits square-planar geometry (Figure 5). The two dinuclear units are interconnected through pyalk hydroxyl bridges linking copper centers from the adjacent dinuclear units at 2.9 Å, while the distance between two copper atoms belonging to the same indolocarbazole scaffold is about 5.5 Å. The structure contains an internal pocket in which two water molecules are coordinated by two copper atoms and two acetate ligands. Strong hydrogen-bonding interactions are present within this pocket. This hydrogen-bonding network is replicated between adjacent tetranuclear units, further stabilizing the inter-molecular packing. The indolocarbazole scaffolds also exhibit strong π-π stacking interactions with an interplanar separation of approximately 3.5 Å. The hydrogen-bonding network and π-π stacking interactions directly translate to the physical properties of the crystals, which exhibit remarkable stability under ambient conditions and poor solubility.

2.3 | Spectroscopic Characterization of Compounds 3 and 4

Compound **3** was characterized by high resolution mass spectrometry (HRMS) and by NMR, IR and UV–vis spectroscopy. In the ^{1}H NMR spectra, the coordination of ligand **2** to the metal

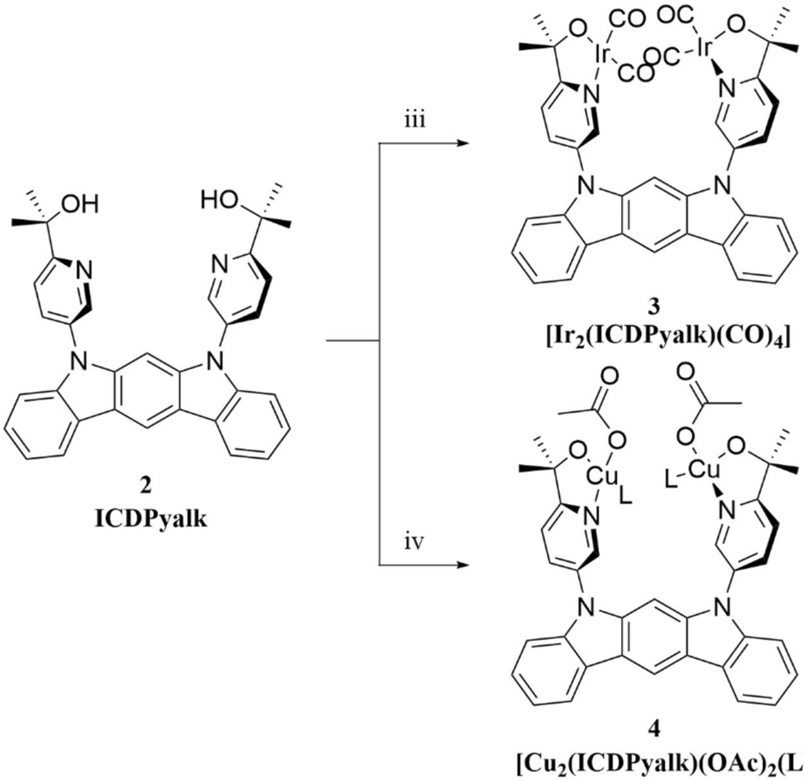

FIGURE 3 | Synthetic pathway for **3** and **4** (L = H_2O, MeOH, or another neutral ligand). (iii) 1. $[Ir(cod)(OMe)]_2$, CH_2Cl_2, rt, 1.5 h; 2. CO bubbling, rt, 15 min. (iv) $Cu(OAc)_2•4H_2O$, $CHCl_3$:MeOH (1:1), rt, overnight.

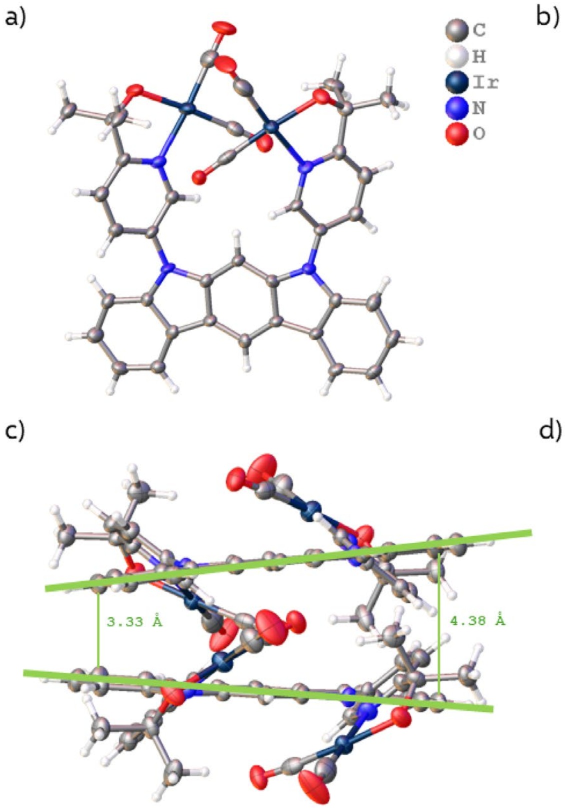

FIGURE 4 | (a) XRD structure of **3**. (b) Ellipsoid representation of **3** highlighting the Ir-Ir′ distance and square-planar geometry angles. (c) Crystal packing of **3**, showing the arrangement of the indolocarbazole planes (in green). (d) Orthogonal view of crystal packing.

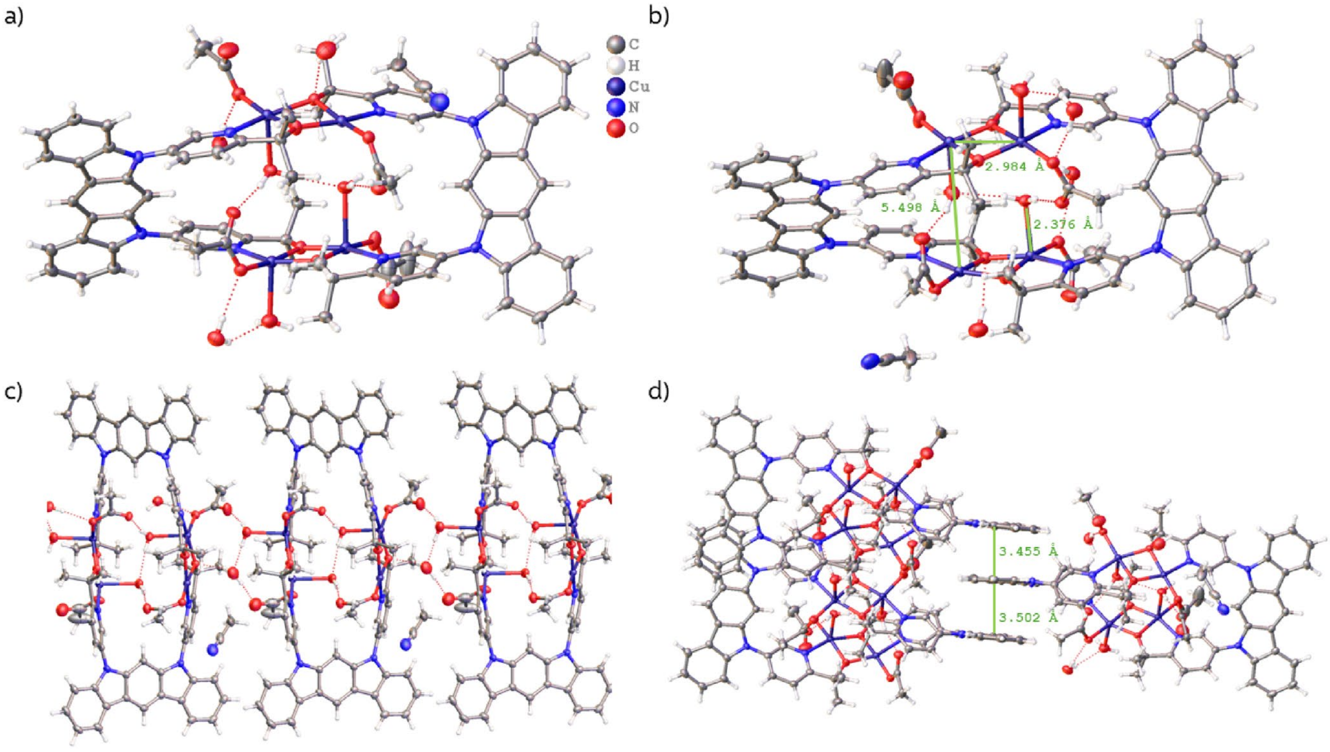

FIGURE 5 | (a) XRD structure of **4**. (b) Ellipsoid representation of **4** highlighting the Cu-Cu′ distances and Cu-H_2O distance. (c) Crystal packing of **4**, showing the intralayer water channel. (d) Crystal packing of **4**, showing the π-π stacking between the indolocarbazoles.

centers was confirmed by the shift of the signals assigned to the pyridine protons to low field by about 0.3 ppm with respect to compound **2** (Figure S3). The formation of two strong symmetrical and asymmetrical stretching bands around 2000 cm^{-1} in the infrared spectrum confirmed the expected insertion of the carbonyls in the last step of the synthetic reaction (Figure S8). The insertion of two iridium centers was confirmed by HRMS, which found the molecular ion at an m/z value of 1021.1317 with an isotopic distribution pattern consistent with having two iridium atoms (Figure S10). UV–vis spectroscopic analysis of **3** in dichloromethane solution revealed limited absorption in the visible region (Figure S13). The most notable difference between **3** and **2** is the enhanced absorption spanning from 450 to 320 nm, which can be attributed to the iridium coordination center. An absorption band at approximately 360 nm, assigned to ligand-centered transitions, appeared slightly blue shifted and with higher intensity than that observed for **2** under identical conditions (Figure S13). Additionally, the band at 300 nm shows a 4-nm blueshift, whereas the higher energy transitions at 288, 276, and 264 nm remain unchanged compared to **2**. The hyperchromic shift suggests the formation of a metal-to-ligand charge transfer band with high absorbance intensity. The molar extinction coefficients of the most relevant transitions are reported in Table 1.

The structural behavior of compound **4** exhibits a notable solid-state versus solution-state discrepancy. The X-ray diffraction analysis reveals a tetranuclear structure in the crystalline form, which would suggest diamagnetic character based on the short 2.9 Å distance between the hydroxyl-bridged Cu(II) centers in the tetranuclear structure. However, the ^{1}H NMR spectrum displays pronounced paramagnetic features in the aromatic region (Figure S6). Proton signals from the indolocarbazole scaffold remain distinguishable due to their distance from the copper centers, suggesting that the tetranuclear assembly dissociates into dinuclear units upon dissolution, giving magnetically independent Cu(II) centers that are not strongly interacting and resulting in a paramagnetic molecule. The presence of the dinuclear species in solution is further supported by HRMS analysis, which found a molecular ion containing only two copper atoms (Figures S11 and S12). Compound **4** exhibited a broad visible absorption band with λ_{max} at 689 nm, consistent with the light blue color of the crystals and the insertion of Cu (Figure S14). The absorption band extended into the near-infrared region beyond the detection limit of the spectrophotometer, precluding accurate determination of the molar extinction coefficient. The molar extinction coefficient was calculated based on the concentration of the dinuclear species, as this is the predominant species of **4** in solution, and allows for better comparison with **2** and **3**, which each contain only one indolocarbazole unit in their structure. Using 500 nm as a baseline reference point, the molar extinction coefficient for the 689-nm d-d transition was estimated to be $(125 \pm 4)\ M^{-1}\,cm^{-1}$. The high-energy part of the spectrum shows transitions associated with ligand **2**, presenting the same λ_{max}. The lower molar extinction coefficients observed for the high-energy transitions of **4** compared to **2** can be associated with the reduction in the intraligand $\pi \rightarrow \pi^*$ transition probability upon coordination to the metal centers, which may affect the symmetry of the indolocarbazole chromophore and perturbs its electronic structure. The FTIR spectrum displays strong absorption bands at approximately 1583 and 1382 cm^{-1}, characteristic of the stretching mode of coordinated acetate, confirming the presence of acetate in the copper coordination sphere (Figure S9) [17].

TABLE 1 | Optical and electrochemical parameters of investigated compounds in solution.

Compound	λ_{max}[a] [nm]	ε[a] [$M^{-1}\,cm^{-1}$]	V_{ox}[b] [V vs. Fc/Fc$^+$] ± 10 [mV]
2	362	21,500 ± 600	0.61
	304	103,200 ± 1500	
3	358	30,600 ± 600	0.54
	300	111,700 ± 500	
4[c]	689	125 ± 4	0.56
	361	9400 ± 100	
	304	37,600 ± 1500	

[a] The UV–vis study was performed in CH_2Cl_2 for compounds **2** and **3**, while the spectra of compound **4** were recorded in $CHCl_3$.
[b] Electrolyte: 0.1 M $TBAPF_6$ in $CHCl_3$.
[c] Molar extinction coefficients were calculated based on the concentration of the dinuclear species in solution.

2.4 | Electrochemical Characterization

Compounds **2**, **3**, and **4** have also been characterized electrochemically, with **2** being investigated to understand the stability of the ligand toward oxidation conditions. The cyclic voltammetry of **2** in *N*,*N*-dimethylformamide (Figure S15a) showed the onset of an irreversible oxidation curve at around 1.1 V versus Ag/AgCl (1.3 V vs. NHE). Differential pulse voltammetry was employed to obtain the potential for oxidation (V_{ox}) in compounds that showed irreversible cyclic voltammetry features (Figure S15b). In the case of **2**, the V_{ox} is 1.46 V versus NHE. To maintain consistency with the preferred solubility of compounds **3** and **4** in $CHCl_3$, electrochemical characterization of **2** was performed in the same solvent (Figure 6a, Table 1). Compound **2** exhibited an irreversible oxidation with V_{ox} of approximately 0.61 V versus Fc/Fc$^+$ (where Fc denotes the ferrocene internal standard) with a returning reducing peak at 0.35 V versus Fc/Fc$^+$. Conversion to the NHE scale employed the commonly reported value of $E^0(Fc^+/Fc) = 0.77$ V versus NHE, recognizing that this value lacks solvent specificity [18]. This yields $V_{ox,\mathbf{2}} = 1.38$ V versus NHE. Due to the oxidation-resistant nature of pyalk [1], we hypothesize that the first oxidation of **2** occurs at the central hydrogen (position 6) of the indolocarbazole scaffold [15]. Following the initial cycle, the electrochemical behavior revealed the formation of a new redox wave at approximately 0.41 V versus Fc/Fc$^+$, which can be attributed to the oxidized **2** species (Figure S16b). Since $V_{ox,\mathbf{2}}$ is higher than the potential required to oxidize $[Ir(pyalk)(CO)_2]$ electrochemically to the blue solution (1.0 V vs. NHE) [7], the ligand looks promising and stable under conditions needed by **3** to oxidize water. The electrochemical response of **3** exhibited an irreversible feature at approximately 0.54 V versus Fc/Fc$^+$, occurring at a lower potential than that of **2** and displaying a distinctly different voltammetric profile (Figure 6b). Consistent with the low potential for oxidation characteristic of iridium dicarbonyl complexes, we attribute this feature to the oxidation of the Ir center accompanied by loss of the dicarbonyl ligands. The irreversibility of the voltammetric trace further supports carbonyl dissociation under oxidative conditions, while the decrease in current intensity at 0.54 V upon repeated cycling suggests decomposition of the precatalytic complex during prolonged oxidation (Figure S17b). Compound **4**, in contrast, exhibited a voltammetric profile like that of **2**, displaying a quasi-reversible oxidation at 0.56 V versus Fc/Fc$^+$ (Figure 6c). The cathodic shift in the potential for oxidation relative to **2** may be attributed to metal coordination.

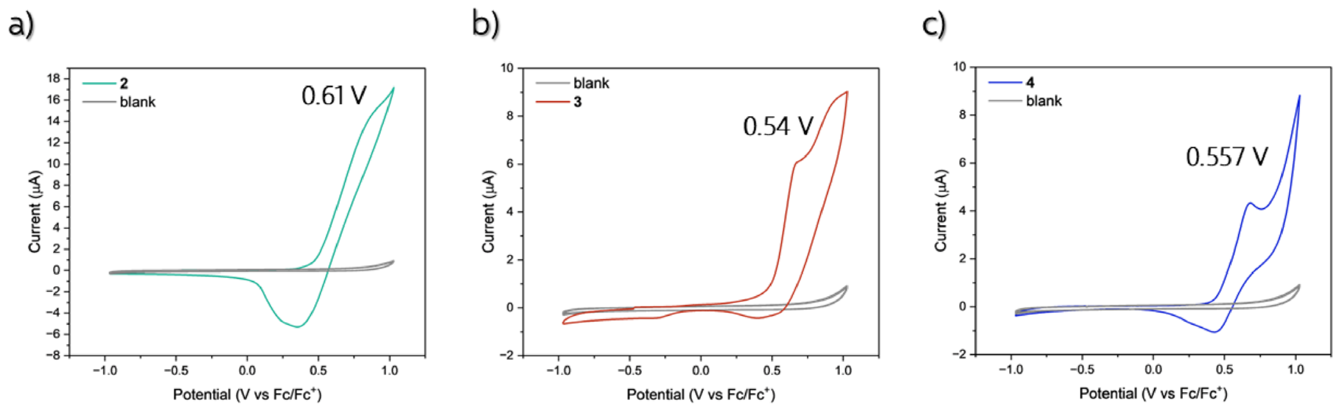

FIGURE 6 | CV in $CHCl_3$ 0.1 M tetrabutylammonium hexafluorophosphate ($TBAPF_6$) of **2** (a), **3** (b), and **4** (c).

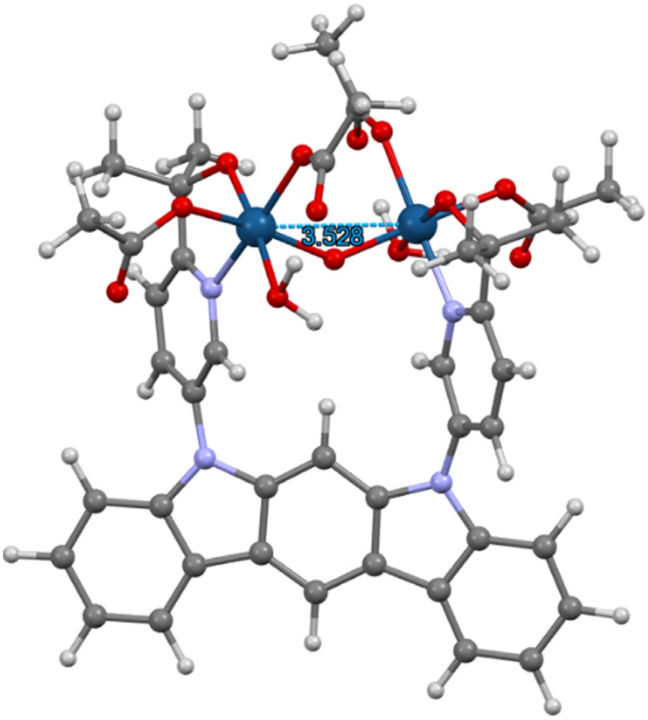

FIGURE 7 | Optimized geometry calculated with DFT. The Ir···Ir separation is highlighted in light blue.

Following the initial cycle, a new feature emerged at 0.3 V versus Fc/Fc$^+$, analogous to the post-oxidation feature observed for **2** but shifted to lower potential (Figure S18b). These results suggest that oxidation of the indolocarbazole scaffold in **4** occurs more readily than metal oxidation. Compared to Cu(pyalk)$_2$, which exhibits an $E_{1/2} = 0.37$ V versus Fc/Fc$^+$ in MeCN, this system lacks the second pyalk coordination around the Cu center, which may account for the shift in redox potential [4].

2.5 | Density Functional Theory Calculations

Density functional theory (DFT) calculations were carried out to evaluate whether a dinuclear iridium complex supported by the **ICDPyalk** ligand can accommodate the proposed μ-oxo-bridged core that is commonly associated with highly active molecular water oxidation catalysts [11]. Structural analyses of blue solution-type iridium catalysts consistently report Ir···Ir separation of approximately 3.5 Å for catalytically relevant μ-oxo-bridged dimers [11]. In contrast, the crystal structure of the precatalyst reported here shows a larger Ir···Ir distance, prompting a computational assessment of whether the dinuclear scaffold can contract to the separation required for μ-oxo bridge formation.

A μ-oxo-bridged dinuclear iridium model was constructed in which each iridium center adopts an octahedral coordination geometry completed by one water ligand and two acetate ligands. Geometry optimizations were performed using unrestricted B3LYP with the SDD effective core potential for iridium and a polarized continuum solvation model for water. The optimized structure preserves the μ-oxo bridge and converges to an Ir···Ir separation of 3.53 Å (Figure 7), in good agreement with reported values for molecular iridium water oxidation catalysts [11, 19, 20]. These results indicate that, despite the larger metal–metal separation observed in the solid-state precatalyst, the dinuclear framework is capable of adopting the shorter Ir···Ir distance required to support the proposed active μ-oxo–bridged motif.

3 | Conclusions

We have developed and validated a versatile ligand platform capable of supporting multinuclear metal complexes across different metal centers through the synthesis of iridium and copper derivatives together with their spectroscopic and electrochemical characterization.

The iridium complex shows strong potential as a precursor to water oxidation catalysis. The ligand imparts rotational flexibility that enables modulation of the Ir···Ir separation, allowing contraction to the ~3.5 Å distance required for formation of a catalytically relevant μ-oxo bridge. This structural flexibility suggests that, although the solid-state precatalyst exhibits a longer metal–metal distance, the framework can access the shorter separation associated with active dinuclear iridium water oxidation motifs. Preliminary results obtained in our group confirm the validity of this strategy with the formation of a blue molecular solution under oxidation conditions (Figure S19). More detailed catalytic and mechanistic studies are currently ongoing.

The copper system displays pronounced structural dynamics. In the solid state, it assembles into a tetranuclear structure featuring a well-defined molecular pocket that positions copper centers in proximity (2.4 Å to the nearest neighbor and ~5 Å along the vertical axis). In solution, however, NMR data indicate dissociation into a paramagnetic dinuclear complex. The tetranuclear structure contains μ-oxo bridges analogous to those found in other multinuclear copper oxidation catalysts [21–24] and enforces Cu···Cu distances comparable to those observed in biological systems such as the methane monooxygenase found in methanotrophic bacteria (which oxidizes methane through two copper centers positioned 2.7 Å apart) [25], and synthetic dicopper oxidation sites, pointing to potential reactivity of our copper complex in oxidative transformations.

Direct catalytic application may be hindered by steric congestion around the μ-oxo bridge and by ligand-centered oxidation occurring before higher copper oxidation states are reached electrochemically. Nevertheless, the rigid pocket defined by the tetranuclear complex has dimensions suitable for binding small diatomic or triatomic guests between two copper centers. This host–guest capability imparts characteristics reminiscent of porous coordination materials and suggests possible utility in gas capture and storage.

Overall, this ligand framework provides a flexible and modular platform for constructing multinuclear metal complexes with tunable metal–metal separations and emergent cavity-like features. These properties open avenues for further exploration in both redox catalysis and functional materials design.

4 | Experimental

General Procedures. All chemicals were purchased from Sigma Aldrich, Ambeed, or Fisher Scientific and used as received. $Cu(AcO)_2 \cdot 4H_2O$ was purchased from Fisher Scientific and used without further purification.

Fourier Transform Infrared (FTIR) Spectroscopy was performed using an Agilent Cary 660 spectrometer.

^{1}H NMR spectra were collected at room temperature on a 400 MHz Bruker NMR spectrometer and referenced to the residual proteo-solvent signals.

High resolution mass spectrometry (HRMS) was performed with a Shimadzu Scientific Instruments QToF 9030 LC–MS system.

UV–Vis absorption spectra were obtained using a Shimadzu 3600 UV–Vis spectrophotometer and a quartz cuvette with a path length of 1 cm.

Electrochemistry. Cyclic voltammetry (CV) and differential pulse voltammetry (DPV) were performed with a Pine WaveNow potentiostat, using a standard three-electrode configuration. A boron-doped diamond (BDD) working electrode was used (3 mm diameter, polished with alumina and rinsed with water, acetone, and acetonitrile then air-dried) with a platinum wire counter electrode. A silver wire was used as a pseudo-reference electrode, and the potential was referenced using a ferrocene internal standard. *N*,*N*-dimethylformamide (DMF) and $CHCl_3$ both with 0.1 M tetrabutylammonium hexafluorophosphate ($TBAPF_6$) were used as electrolytes. The potentials measured versus Fc/Fc^+ are converted to normal hydrogen electrode (NHE) by the addition of +0.77 V [18]. All CVs were measured with a scan rate of 150 mV/s, if not specified in the figure caption. DPV used a pulse of 5 mV height, 100 ms width, 500 ms period, and 5 mV increment.

Density functional theory calculations. Geometry optimizations were carried out using density functional theory (DFT) with the unrestricted B3LYP (UB3LYP) functional [26]. Iridium atoms were treated using the Stuttgart-Dresden effective core potential (SDD) [27], while all remaining atoms were described using a double-ξ basis set. Solvent effects were included using the polarizable continuum model (PCM) with water as the dielectric medium [28], and Grimme's D3 empirical dispersion correction was applied [29]. All structures were fully optimized without symmetry constraints using the Gaussian 16 software package [30]. Optimized geometries were visualized using Mercury software [31].

Crystallographic data. Low-temperature diffraction data (ω-scans) were collected on a Rigaku Synergy-S diffractometer coupled to a HyPix-Arc 100 detector with Cu Kα ($\lambda = 1.54178$ Å) for the structure of syn-24005. The diffraction images were processed and scaled using Rigaku Oxford Diffraction software CrysAlisPro [32]. The structure was solved with SHELXT and was refined against F^2 on all data by full-matrix least squares with SHELXL [33]. All non-hydrogen atoms were refined anisotropically. Hydrogen atoms were included in the model at geometrically calculated positions and refined using a riding model. The isotropic displacement parameters of all hydrogen atoms were fixed to 1.2 times the U value of the atoms to which they are linked (1.5 times for methyl groups). O—H hydrogen atoms were located from the difference map and refined semi-freely. When a mask was used, it was computed using the Olex2 implementation of SQUEEZE [34]. Crystallographic data for the structures reported in this paper have been deposited with the Cambridge Crystallographic Data Centre as supplementary publication no. CCDC2521680, CCDC2521681, and CCDC2521435. Copies of the data can be obtained free of charge on application to CCDC, 12 Union Road, Cambridge CB2 1EZ, UK [fax.: (internat.) + 441,223/336–033; e-mail: deposit@ccdc.cam.ac.uk].

Acknowledgments

This work was supported by the U.S. Department of Energy, Chemical Sciences, Geosciences, and Biosciences Division, Office of Basic Energy Sciences, Office of Science (grant DE-FG02-07ER15909). Additional support was provided by a generous donation from the TomKat Charitable Trust. This research made use of the Chemical and Biophysical Instrumentation Center at Yale University (RRID:SCR_021738). HRMS equipment was purchased with funds from Yale University and the NSF MRI grant CHE-1828190. The authors thank Dr. Fabian Menges for help with HRMS analysis and Prof. Robert H. Crabtree for useful discussion.

Funding

This work was supported by the U.S. Department of Energy, DE-FG02-07ER15909.

Data Availability Statement

The data that support the findings of this study are openly available in Cambridge Crystallographic Data Centre at https://www.cambridgenetwork.co.uk/directories/companies/153, reference number CCDC2521680, CCDC2521681, CCDC2521435.

References

1. T. K. Michaelos, D. Y. Shopov, S. B. Sinha, et al., "A Pyridine Alkoxide Chelate Ligand That Promotes Both Unusually High Oxidation States and Water-Oxidation Catalysis," *Accounts of Chemical Research* 50 (2017): 952–959.

2. E. V. Sackville, G. Kociok-Köhn, and U. Hintermair, "Ligand Tuning in Pyridine-Alkoxide Ligated Cp*IrIIIOxidation Catalysts," *Organometallics* 36 (2017): 3578–3588.

3. K. J. Fisher, M. L. Feuer, H. M. C. Lant, B. Q. Mercado, R. H. Crabtree, and G. W. Brudvig, "Concerted Proton-Electron Transfer Oxidation of Phenols and Hydrocarbons by a High-Valent Nickel Complex," *Chemical Science* 11 (2020): 1683–1690.

4. K. J. Fisher, H. R. Kelly, C. C. Cody, et al., "Metal-Dependent Asynchronicity of Concerted Proton–Electron Transfer to a High-Valent Copper(III) Complex and Its Nickel(III) Analogue," *Inorganic Chemistry* 64 (2025): 14552–14565.

5. K. J. Fisher, K. L. Materna, B. Q. Mercado, R. H. Crabtree, and G. W. Brudvig, "Electrocatalytic Water Oxidation by a Copper(II) Complex of an Oxidation-Resistant Ligand," *ACS Catalysis* 7 (2017): 3384–3387.

6. U. Hintermair, S. W. Sheehan, A. R. Parent, et al., "Precursor Transformation During Molecular Oxidation Catalysis With Organometallic Iridium Complexes," *Journal of the American Chemical Society* 135 (2013): 10837–10851.

7. D. L. Huang, R. Beltrán-Suito, J. M. Thomsen, et al., "New Ir Bis-Carbonyl Precursor for Water Oxidation Catalysis," *Inorganic Chemistry* 55 (2016): 2427–2435.

8. T. K. Michaelos, H. M. C. Lant, L. S. Sharninghausen, et al., "Catalytic Oxygen Evolution From Manganese Complexes With an Oxidation-Resistant N,N,O-Donor Ligand," *ChemPlusChem* 81 (2016): 1129–1132.

9. U. Hintermair, S. M. Hashmi, M. Elimelech, and R. H. Crabtree, "Particle Formation During Oxidation Catalysis With Cp* Iridium Complexes," *Journal of the American Chemical Society* 134 (2012): 9785–9795.

10. G. Luciani, C. Decavoli, R. H. Crabtree, and G. W. Brudvig, "Water Oxidation Catalysis by an Iridium Complex Stabilized With an N,N,O-Donor Tripodal Ligand," *Energy & Fuels* 39 (2025): 6549–6558.

11. K. R. Yang, A. J. Matula, G. Kwon, et al., "Solution Structures of Highly Active Molecular Ir Water-Oxidation Catalysts From Density Functional Theory Combined With High-Energy X-Ray Scattering and EXAFS Spectroscopy," *Journal of the American Chemical Society* 138 (2016): 5511–5514.

12. G. Hu, R. H. Crabtree, and G. W. Brudvig, "Organometallic Complexes as Preferred Precursors to Form Molecular Ir(Pyalk) Coordination Complexes for Catalysis of Oxygen Evolution," *Inorganica Chimica Acta* 526 (2021): 120507.

13. B. Rudshteyn, K. J. Fisher, H. M. C. Lant, et al., "Water-Nucleophilic Attack Mechanism for the CuII(Pyalk)2Water-Oxidation Catalyst," *ACS Catalysis* 8 (2018): 7952–7960.

14. M. Jian, Z. Song, X. Chen, J. Zhao, B. Xu, and Z. Chi, "Afterglows From the Indolocarbazole Families," *Chemical Engineering Journal* 429 (2022): 132346.

15. T. Janosik, A. Rannug, U. Rannug, N. Wahlström, J. Slätt, and J. Bergman, "Chemistry and Properties of Indolocarbazoles," *Chemical Reviews* 118 (2018): 9058–9128.

16. J. K. Kwon, J. H. Cho, Y.-S. Ryu, S. H. Oh, and E. K. Yum, "N-Arylation of Carbazole by Microwave-Assisted Ligand-Free Catalytic CuI Reaction," *Tetrahedron* 67 (2011): 4820–4825.

17. A. M. Al-Sabagh, F. Z. Yehia, A. M. F. Eissa, et al., "Cu- and Zn-Acetate-Containing Ionic Liquids as Catalysts for the Glycolysis of Poly(Ethylene Terephthalate)," *Polymer Degradation and Stability* 110 (2014): 364–377.

18. A. J. Bardand and L. R. Faulkner, *Electrochemical Methods: Fundamentals and Applications*, 2nd ed. (John Wiley & Sons, Inc, 2001).

19. L. S. Sharninghausen, S. B. Sinha, D. Y. Shopov, et al., "High Oxidation State Iridium Mono-μ-Oxo Dimers Related to Water Oxidation Catalysis," *Journal of the American Chemical Society* 138 (2016): 15917–15926.

20. G. Hu, J. L. Troiano, U. T. Tayvah, et al., "Accessing Molecular Dimeric Ir Water Oxidation Catalysts From Coordination Precursors," *Inorganic Chemistry* 60 (2021): 14349–14356.

21. S. I. Chan, C. Y. C. Chien, C. S. C. Yu, P. Nagababu, S. Maji, and P. P. Y. Chen, "Efficient Catalytic Oxidation of Hydrocarbons Mediated by Tricopper Clusters Under Mild Conditions," *Journal of Catalysis* 293 (2012): 186–194.

22. S. I. Chan, Y.-J. Lu, P. Nagababu, et al., "Efficient Oxidation of Methane to Methanol by Dioxygen Mediated by Tricopper Clusters," *Angewandte Chemie, International Edition* 52 (2013): 3731–3735.

23. C.-C. Liu, D. Janmanchi, D.-R. Wen, et al., "Catalytic Oxidation of Light Alkanes Mediated at Room Temperature by a Tricopper Cluster Complex Immobilized in Mesoporous Silica Nanoparticles||," *ACS Sustainable Chemistry & Engineering* 6 (2018): 5431.

24. Y.-F. Tsai, T. Natarajan, Z.-H. Lin, et al., "Voltage-Gated Electrocatalysis of Efficient and Selective Methane Oxidation by Tricopper Clusters Under Ambient Conditions," *Journal of the American Chemical Society* 144 (2022): 9695–9706.

25. W. H. Chang, H. H. Lin, I. K. Tsai, et al., "Copper Centers in the Cryo-EM Structure of Particulate Methane Monooxygenase Reveal the Catalytic Machinery of Methane Oxidation," *Journal of the American Chemical Society* 143 (2021): 9922–9932.

26. P. J. Stephens, F. J. Devlin, C. F. Chabalowski, and M. J. Frisch, "Ab Initio Calculation of Vibrational Absorption and Circular Dichroism Spectra Using Density Functional Force Fields," *Journal of Physical Chemistry* 98 (1994): 11623–11627.

27. I. S. Alkhaibari, X. Zhang, J. Zhao, et al., "Tuning Excited State Character in Iridium(III) Photosensitizers and Its Influence on TTA-UC," *Inorganic Chemistry* 63 (2024): 9931–9940.

28. J. Tomasi, B. Mennucci, and R. Cammi, "Quantum Mechanical Continuum Solvation Models," *Chemical Reviews* 105 (2005): 2999–3094.

29. S. Grimme, J. Antony, S. Ehrlich, and H. Krieg, "A Consistent and Accurateab Initioparametrization of Density Functional Dispersion Correction (DFT-D) for the 94 Elements H-Pu," *Journal of Chemical Physics* 132 (2010): 132.

30. M. J. Frisch, G. W. Trucks, H. B. Schlegel, et al., "Gaussian 16 Rev. C.01" Wallingford, CT, 2016.

31. C. F. Macrae, I. Sovago, S. J. Cottrell, et al., "Mercury 4.0: From Visualization to Analysis, Design and Prediction," *Journal of Applied Crystallography* 53 (2020): 226–235.

32. Rigaku OD, "CrysAlisPro," The Woodlands, TX, 2015.

33. G. Sheldrick, "A Short History of SHELX," *Acta Crystallographica, Section A: Foundations of Crystallography* 64 (2008): 112–122.

34. B. Rees, L. Jenner, and M. Yusupov, "Bulk-Solvent Correction in Large Macromolecular Structures," *Acta Crystallographica Section D* 61 (2005): 1299–1301.

Supporting Information

Additional supporting information can be found online in the Supporting Information section. **Figure S1:** ^{1}H NMR spectrum of **1** in $CDCl_3$. **Figure S2:** ^{1}H NMR spectrum of **2** in CD_2Cl_2. **Figure S3:** ^{1}H NMR spectrum of **3** in CD_2Cl_2. **Figure S4:** ^{13}C NMR spectrum of **3** in CD_2Cl_2. **Figure S5:** ^{13}C

DEPT-135 NMR spectrum of **3** in CD_2Cl_2. **Figure S6:** ^1H NMR spectrum of **4** in $CDCl_3$. **Figure S7:** FTIR spectrum of **2**. **Figure S8:** FTIR spectrum of **3**. **Figure S9:** FTIR spectrum of **4**. **Figure S10:** HRMS of **3**. (a) full spectrum; (b) zoom on the region of interest; (c) calculated spectrum of the region of interest. **Figure S11:** HRMS of **4**. **Figure S12:** Zoom of the HRMS of **4** for $C_{36}H_{31}Cu_2N_4O_4^+$ found (top) and calculated (bottom). **Figure S13:** UV-vis spectra of **2** and **3** in CH_2Cl_2 (5×10^{-6} M). **Figure S14:** (a) UV-vis spectra of **4** and **2** in $CHCl_3$ (10^{-5} M); (b) Zoom on the 689-nm transitions in the UV-vis spectrum of **4** in $CHCl_3$ (10^{-3} M). **Figure S15:** (a) CV and (b) DPV of **2** in DMF 0.1 M tetrabutylammonium hexafluorophosphate ($TBAPF_6$). Ferrocene is present as internal reference for DPV measurement. **Figure S16:** CVs of **2** in $CHCl_3$ 0.1 M $TBAPF_6$ with separation between the first cycle (a) and the second and third cycles (b). **Figure S17:** CVs of **3** in $CHCl_3$ 0.1 M $TBAPF_6$ with separation between the first cycle (a) and the second and third cycles (b). **Figure S18:** CVs of **4** in $CHCl_3$ 0.1 M $TBAPF_6$ with separation between the first cycle (a) and the second and third cycles (b). **Figure S19:** Photo of the oxidized compound **3** turning into a blue molecular solution. Catalytic studies are ongoing. **Figure S20:** The complete numbering scheme of syn-24005 (complex **3**) with 50% thermal ellipsoid probability levels. The hydrogen atoms are shown as circles for clarity. **Figure S21:** The complete numbering scheme of syn-23125 (complex **4**, crystal form 1) with 50% thermal ellipsoid probability levels. The hydrogen atoms are shown as circles for clarity. **Figure S22:** The complete numbering scheme of syn-25087 (complex **4**, crystal form 2) with 50% thermal ellipsoid probability levels. The hydrogen atoms are shown as circles for clarity. **Table S1:** DFT-optimized Cartesian coordinates of the μ-oxo-bridged dinuclear iridium complex. **Table S2:** Crystal data and structure refinement for syn-24005. **Table S3:** Fractional atomic coordinates ($\times 10^4$) and equivalent isotropic displacement parameters ($Å^2 \times 10^3$) for syn-24005. U_{eq} is defined as 1/3 of the trace of the orthogonalized U_{IJ} tensor. **Table S4:** Bond lengths [**Å**] for syn-24005. **Table S5:** Bond Angles [°] for syn-24005. **Table S6:** Anisotropic displacement parameters ($Å^2 \times 10^3$) for syn-24005. The Anisotropic displacement factor exponent takes the form: $-2\pi^2[h^2a^{*2}U_{11} + 2hka^*b^*U_{12}+...]$. **Table S7:** Hydrogen Atom Coordinates ($Å \times 10^4$) and Isotropic Displacement Parameters ($Å^2 \times 10^3$) for syn 24005. **Table S8:** Torsion angles [°] for syn-24005. **Table S9:** Crystal data and structure refinement for syn-23125. **Table S10:** Fractional atomic coordinates ($\times 10^4$) and equivalent isotropic displacement parameters ($Å^2 \times 10^3$) for syn-23125. U_{eq} is defined as 1/3 of the trace of the orthogonalized U_{IJ} tensor. **Table S11:** Bond lengths [Å] for syn-23125. **Table S12:** Bond angles [°] for syn-23125. **Table S13:** Anisotropic displacement parameters ($Å^2 \times 10^3$) for syn-23125. The anisotropic displacement factor exponent takes the form: $-2\pi^2[h^2a^{*2}U_{11} + 2hka^*b^*U_{12}+...]$. **Table S14:** Torsion angles [°] for syn-23125. **Table S15:** Hydrogen atom coordinates ($Å \times 10^4$) and isotropic displacement parameters ($Å^2 \times 10^3$) for syn-23125. **Table S16:** Hydrogen bonds [Å] and angles [°] for syn-23125. **Table S17:** Crystal data and structure refinement for syn-25087. **Table S18:** Atomic coordinates ($\times 10^4$) and equivalent isotropic displacement parameters ($Å^2 \times 10^3$) for syn-25087. U_{eq} is defined as one third of the trace of the orthogonalized U^{IJ} tensor. **Table S19:** Bond lengths [Å] for syn-25087. **Table S20:** Bond angles [°] for syn-25087. **Table S21:** Anisotropic displacement parameters ($Å^2 \times 10^3$) for syn-25087. The anisotropic displacement factor exponent takes the form: $-2\pi^2[h^2a^{*2}U_{11} + 2hka^*b^*U_{12}+...]$. **Table S22:** Hydrogen atom coordinates ($Å \times 10^4$) and Isotropic displacement parameters ($Å^2 \times 10^3$) for syn-25087. **Table S23:** Torsion angles [°] for syn-25087. **Table S24:** Hydrogen bonds for syn-25087 [Å and °].

Biographies

Cristina Decavoli is a postdoctoral researcher at the Energy Sciences Institute at Yale University, working under the supervision of Prof. Gary Brudvig. She received her Ph.D. in Materials Science and Nanotechnology from the University of Milano-Bicocca, Italy (2022). Her research focuses on molecular water oxidation catalysts and organic dyes for the development of new technologies for solar-driven water splitting applications. Her scientific journey has also been shaped, indirectly, by the legacy of Prof. Sunney Chan, whose mentorship of Prof. Brudvig helped forge the scientific foundation and values that continue to guide the group today.

Jana Jelušić is a Ph.D. candidate in Chemistry at Yale University, working under the supervision of Prof. Gary Brudvig and Prof. Victor Batista. Her research focuses on computational and electrochemical studies of catalytic pathways for the reduction of nitrogen oxyanions to ammonia, with an emphasis on carbon-based materials and transition metal systems for sustainable energy applications. Although she did not work directly with Prof. Sunney Chan, his influence is reflected through his mentorship of Prof. Brudvig and the scientific lineage of the group, which continues to shape her approach to research and mentorship.

Sebastian M. Krajewski is the crystallographer at the Chemical and Biophysical Instrumentation Center in the Department of Chemistry at Yale University. He received his Ph.D. in Chemistry from the University of Washington, Seattle (2025). His work as crystallographer and facility manager at Yale centers on advancing the depth and breadth of structural science using techniques such as electron diffraction. He recognizes Sunney Chan as an exemplary scientist whose works often made extensive usage of crystallography.

Victor S. Batista is the John Gamble Kirkwood Professor of Chemistry at Yale University. He received his B.Sc. in Chemistry from the Universidad de Buenos Aires (1989) and his Ph.D. in Chemistry from Boston University (1996), working under the direction of Prof. David F. Coker. Following postdoctoral research with Prof. William H. Miller at the University of California, Berkeley and Prof. Paul Brumer at the University of Toronto, he joined the Yale faculty in 2001, where he has since held multiple leadership and distinguished professorship roles. Batista has received numerous awards, including the NSF CAREER Award, the Camille Dreyfus Teacher-Scholar Award, and a Fulbright Fellowship. He is a Fellow of the Royal Society of Chemistry and a member of several professional societies. His research involves the development and application of theoretical and computational methods to study photoinduced processes, quantum dynamics, and catalytic mechanisms in complex systems, including natural and artificial photosynthesis. The broader scientific context of this work reflects the lasting influence of Sunney Chan on the field. His contributions and mentorship lineage have helped shape the intellectual foundations and values that continue to guide research in this area.

Gary W. Brudvig is the Benjamin Silliman Professor of Chemistry, Professor of Molecular Biophysics & Biochemistry, and Director of the Yale Energy Sciences Institute at Yale University. He received his B.S. (1976) from the University of Minnesota, his Ph.D. (1981) from Caltech working under the direction of Sunney Chan, and was a Miller Postdoctoral Fellow at the University of California, Berkeley from 1980 to 1982. Professor Brudvig has been on the faculty at Yale since 1982 and served as Chair of the Chemistry Department from 2003 to 2009 and 2015 to 2018. He is a member of the American Academy of Arts & Sciences and the U.S. National Academy of Sciences. Since 2012, Brudvig has been the Director of the Energy Sciences Institute located at Yale's West Campus where he oversees the development of new research programs and facilities related to renewable energy, alternative fuels, and materials science. His research involves study of the chemistry of solar energy conversion in photosynthesis and work to develop artificial bioinspired systems for solar fuel production. I want to say a few words on my background with Sunney Chan and the tremendous impact he has had on my career. On top of being one of the preeminent biophysical chemists in the world, Sunney Chan had a rare level of commitment to the training of students. Sunney was a fantastic mentor, supporter and role model for me. I have followed his example in my independent career. I can't thank him enough for all his guidance and support.